Energy &
Environmental
Science

ROYAL SOCIETY
OF CHEMISTRY

PAPER

View Article Online
View Journal | View Issue

Cite this: *Energy Environ. Sci.*, 2023, **16**, 2611

Regulating active hydrogen adsorbed on grain boundary defects of nano-nickel for boosting ammonia electrosynthesis from nitrate†

Jian Zhou,[a] Ming Wen, *[a] Rong Huang,[b] Qingsheng Wu,[a] Yixing Luo,[a] Yakun Tian,[a] Guangfeng Wei[a] and Yongqing Fu[c]

Received 20th December 2022,
Accepted 14th April 2023

DOI: 10.1039/d2ee04095f

rsc.li/ees

The electrochemical nitrate reduction reaction (NitRR) into ammonia is a promising route for sustainable ammonia synthesis under ambient conditions. Since the hydrogen evolution reaction (HER) is its main competing reaction, many researchers apply materials (*e.g.*, copper-based materials) which are inert in water splitting for enhancing the conversion efficiency of nitrate into ammonia. The HER active metals (*e.g.*, nickel) are usually considered unsuitable for such applications. However, the NitRR relies strongly on H* which is produced from water splitting, and HER active metals such as Ni can produce massive H* for the consumption of the intermediates. Therefore, HER active metals could be promising candidates for the NitRR if the destination of H* can be well regulated, but this has not been well investigated. Herein, a strategy of grain boundary (GB) defect engineering of nickel nanoparticles has been developed to electrocatalyze the NitRR, which achieves a high NH_3 rate of 15.49 mmol h^{-1} cm^{-2} with a faradaic efficiency of 93.0%. This NH_3 rate, to the best of our knowledge, is much higher than those reported for the commonly used materials including copper or noble metal-based catalysts. Both experimental and computational simulation results reveal that the GBs can significantly suppress the HER by regulating the H* to favor its consumption in the NitRR pathway rather than forming hydrogen. The adsorption of NO_3* can also be promoted, thus effectively enhancing the key rate-determining step of NO_3* to NO_2*.

Broader context

Nitrate electroreduction (NitRR) to ammonia is one promising way to synthesize ammonia and has received more and more attention. However, the NitRR to ammonia involves multiple steps and thus suffers from a poor faradaic efficiency and a low NH_3 rate. The most active material is copper due to its intrinsic properties. The other metals are investigated rarely and show a relatively low efficiency, especially the HER active metal, because the HER is the main competing reaction. However, in the NitRR, the H* assisted way plays an important role in ammonia selectivity. The HER active metal can supply massive H* as the potential source for the consumption of the intermediates and favor the generation of ammonia. So, the HER active metal can also be a promising candidate even though the HER is the main competing reaction. The problem is preventing H* from dissociation to form hydrogen and make sure it is being consumed in the NitRR. Here we demonstrated that the grain boundary defect engineered nickel (an intensively investigated metal in the HER) nanoparticles can significantly promote the NitRR *via* regulating the adsorption behavior of H* and the main intermediates. Such a catalyst displays a superior NH_3 rate which overcomes those of almost all reported materials including copper and noble metal derived ones. The catalyst design methodology proposed here may offer a new perspective for the NitRR.

1 Introduction

Ammonia is one of the most fundamental feedstocks used for fertilizers, medicines, pesticides and many other chemical products.[1,2] Recently it has been explored as a promising clean energy carrier because of its high energy density (4.3 kW h kg^{-1}) and harmless combustion products (N_2 and H_2O).[3,4] However, large-scale synthesis of ammonia still relies on the conventional Haber–Bosch (H–B) process,[5] which requires high

---

[a] *School of Chemical Science and Engineering, State Key Laboratory of Pollution Control and Resource Reuse, Shanghai Key Laboratory of Chemical Assessment and Sustainability, Tongji University, Shanghai, 200092, China. E-mail: m_wen@tongji.edu.cn; Tel: +86 21-65981097*

[b] *Key Laboratory of Polar Materials and Devices (MOE) and Department of Electronics, School of Physics and Electronic Science, East China Normal University, Shanghai 200062, China*

[c] *Faculty of Engineering and Environment, Northumbria University, Newcastle upon Tyne NE99, UK*

† Electronic supplementary information (ESI) available. See DOI: **https://doi.org/10.1039/d2ee04095f**

temperature and high pressure to break the extremely stable N≡N (941 kJ mol^{-1}) bond, and therefore consumes a huge amount of fossil fuel and emits massive CO_2.[6] Considering the shortcomings of the H–B process, it is crucial to develop sustainable routes as a supplement to the H–B process to meet the increasing industrial demands for ammonia.

The electrochemical nitrate reduction reaction (NitRR) has recently been proposed as one alternative route to synthesize ammonia under ambient conditions.[3] In this process, it is much easier to break the N–O bond (204 kJ mol^{-1}), rather than breaking the strong N≡N bond.[7] The universally existing nitrate contaminates in industrial wastewater ranging from ∼0.8 mM to ∼2 M can be used as resources.[3] Moreover, this NitRR route has also been regarded as one valid way to mitigate the nitrate pollution in the hydrosphere and further rebalance the perturbed nitrogen cycle,[8–10] which is beneficial for sustainable development.[11] However, the electrochemical NitRR to ammonia is a very complicated process. It contains the transfer of 8 electrons and 9 protons, during which many possible intermediates and products can be formed.[12] What is more, the main competing process, *i.e.*, the hydrogen evolution reaction (HER), cannot be effectively suppressed at a high applied potential. As a consequence, the conversion from nitrate into ammonia still suffers from a low NH_3 rate (most of the recently reported NH_3 rates are still under 2 mmol h^{-1} cm^{-2}) and a poor faradaic efficiency (FE),[13] both of which are the main barriers for its commercialization.[11]

To date, considerable effort has been made to explore new types of catalysts for improving the efficiency and selectivity of the NitRR process, for example, metals/metal oxides,[14–18] alloys/bimetals,[19–23] metal phosphides,[24–26] and single atom catalysts.[13,27–30] Among them, copper or noble metal-based materials have been investigated intensively because of their superior intrinsic properties for nitrate reduction. On the other hand, other metal-based materials are rarely explored, especially some HER active metals (*e.g.*, nickel). They are usually considered unsuitable for such applications, since the HER is its main competing reaction.[20,31,32] However, the NitRR process relies heavily on H* which is produced from H_2O splitting.[12,33,34] The conversion efficiency of nitrate into ammonia will not be promoted significantly if the water splitting has been severely suppressed, as it cannot provide enough H* for the NitRR. To solve this problem, a strategy has been developed which introduces new elements (such as Rh and Au) to ensure the acquisition of enough H* but avoid massive H* production in order to suppress the HER, thus achieving a high NH_3 rate.[35,36] Inspired by this idea, we believe that it is promising to construct efficient catalysts based on the materials that perform well in water splitting as they can produce massive H* as a potential source for the consumption of the intermediates in the NitRR pathway. Water splitting should be utilized rather than being suppressed, and the metals that perform well in the HER could also be promising candidates. Of course, the major challenge for this strategy is how to prevent the formation of hydrogen from H*.

In this work, we proposed a strategy to construct grain boundary (GB) defect engineered nickel nanoparticles (Ni NPs) on carbon cloth through a controllable electrodeposition process for promoting the conversion efficiency of nitrate to ammonia. Owing to the HER activity of Ni,[37–39] massive H* can be produced on its surface. However, the GB regions have a high H* retention capacity and thus the H* cannot be easily released to form hydrogen but be transferred to the adjacently adsorbed intermediates in the NitRR pathway, which is beneficial for the intermediates to acquire enough H*. This mechanism can be verified by both experimental and computational simulation results. What is more, such a structure of GB defect engineered Ni NPs is favorite for promoting and accelerating the rate-determining step (RDS) of NO_3* to NO_2*. Owing to the synergetic effects discussed above, our synthesized GB Ni NPs displayed a high NH_3 rate of 15.49 mmol h^{-1} cm^{-2} with an FE of 93.0%. Furthermore, prolonged electrocatalysis for 30 h was performed using a chronopotentiometry method at 2 A cm^{-2}. The catalytic activity for nitrate reduction decreases only slightly over 30 h, which indicates outstanding stability of this structure.

2 Results and discussion

2.1 Synthesis process of GB defect engineered Ni NPs

The GB Ni NPs were synthesized *via* the electrodeposition method as illustrated in Fig. 1. In this process, the HER and

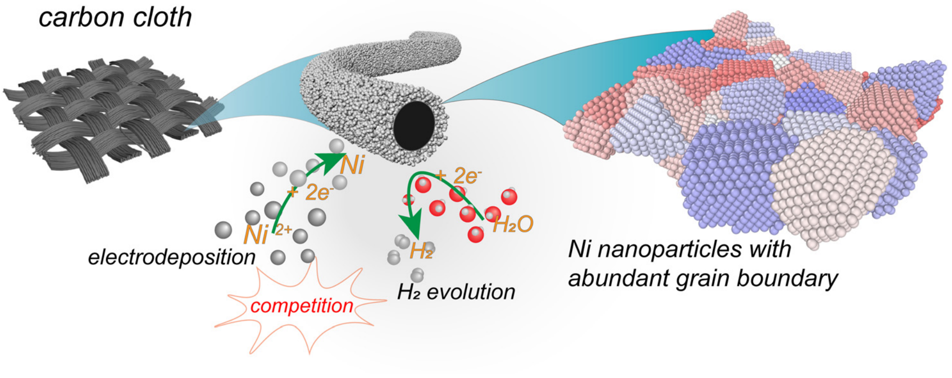

Fig. 1 Schematic diagram for the fabrication processes of GB defect engineered Ni NPs.

Ni deposition processes take place simultaneously on carbon cloth which is applied as the cathode. Therefore, the ordered deposition of Ni^{2+} ions is disturbed by the HER, which results in the formation of numerous GB defects.[40] Obviously, a strong competition between the HER and Ni deposition will determine the final outcomes. When the concentration of Ni^{2+} ions is fixed, the applied electrodeposition potential becomes the main factor for the generation of GB defects.[41–43] As the potential is increased from −0.6 V to −2.0 V against a saturated calomel electrode (SCE), the competition effect can be revealed from the linear sweep voltammetry (LSV) curve (Fig. S1, ESI†). In the beginning, the current change is associated with the conversion of Ni^{2+} to Ni, in which the electrodeposition is the dominant reaction. As the potential is increased to about −1 V, there is an apparent change in the trend of LSV curves, which indicates the beginning of the HER process. The onset potential of the HER becomes more negative if the carbon cloth is deposited with Ni NPs in advance, which clearly reveals that the obtained Ni NPs with GB defects show an inhibition effect on the HER. When the potential is further increased to −1.8 V, massive bubbles are observed on the cathode, and the dominant reaction becomes the HER.[41,42] Therefore, the competition degree of these two processes may reach a peak under a certain potential in the range from −1 to −1.8 V, where abundant GB defects can be formed. In this study, by applying the electrodeposition potential from −1.8 V with an increase step of 0.2 V, several samples were synthesized to optimize the electrodeposition potentials, namely Ni-NPs-1.8, 1.6, and 1.4.

2.2 Characterization of GB defect engineered Ni NPs

Fig. 2 shows the characterization results of the as-synthesized Ni NPs on carbon cloth. From the SEM images, the carbon

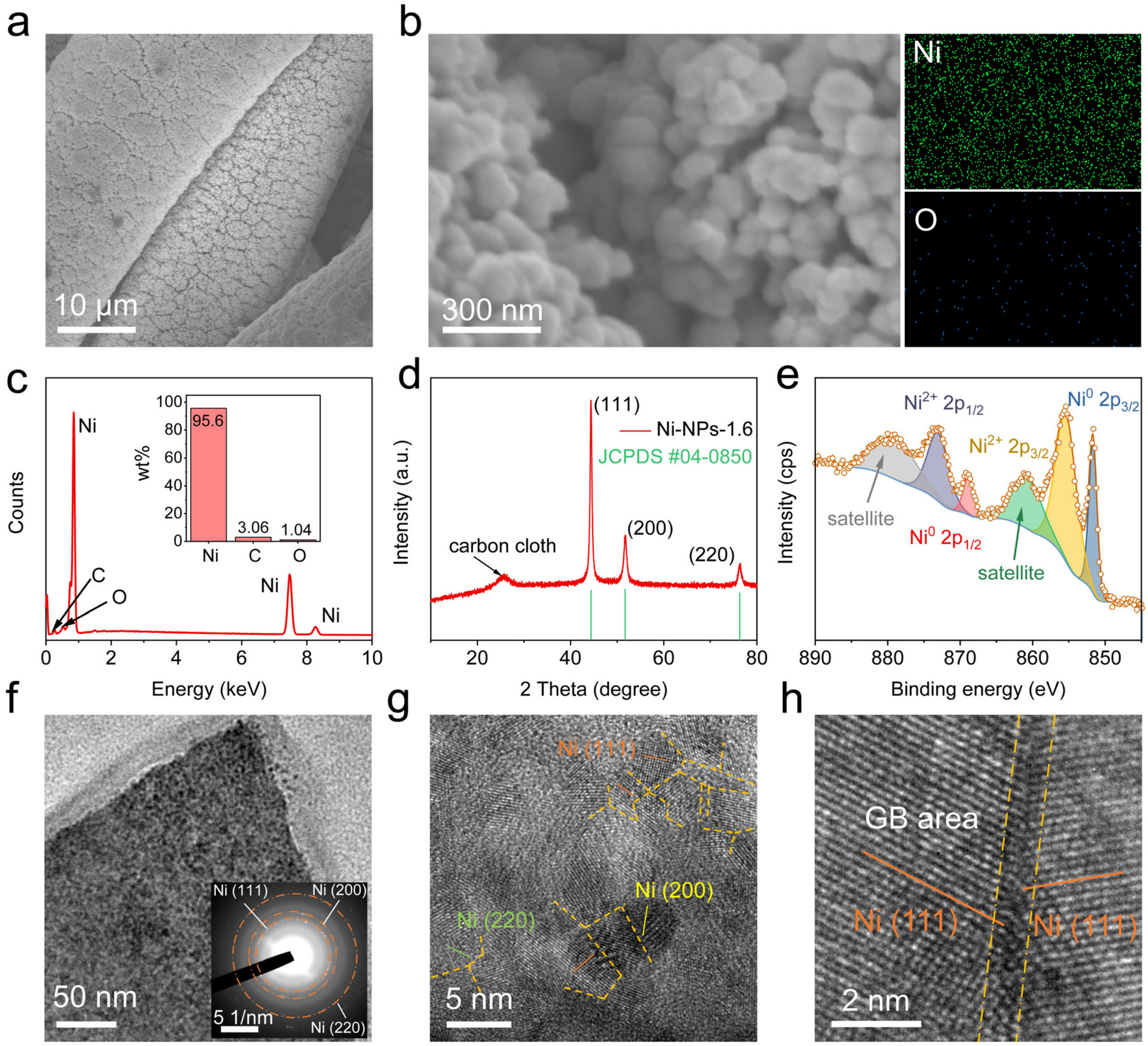

Fig. 2 Characterization of Ni-NPs-1.6. (a and b) SEM images with elemental mapping and (c) elemental composition estimated by EDX. (d) XRD pattern. (e) Ni 2p XPS spectrum. (f) TEM image in low magnification with the inset showing the SAED pattern. (g) HRTEM image (the GBs are marked with a dashed line, and the orientations of different planes are marked with a solid line, orange for Ni(111), yellow for Ni(200) and green for Ni(220)). (h) STEM-HAADF image of one specific GB region.

fibers are wrapped by numerous nanoparticles with a thickness of ~5.6 μm (Fig. 2a, b and Fig. S2, ESI†). Samples of Ni-NPs-1.4 and 1.8 show similar morphology (Fig. S3 and S4, ESI†). These nanoparticles are not densely packed, which is beneficial for efficient ion transport, larger surface areas and more exposed active sites. The proportion of the elemental composition estimated using an energy dispersive X-ray spectrometer (EDS) (Fig. 2c) shows 95.6 wt% Ni with slight oxygen and carbon (from the carbon cloth) confirming that the composition of the sample is mainly Ni. The X-ray diffraction (XRD) spectrum of the Ni-NPs-1.6 (Fig. 2d) also shows the phase of Ni. The peaks at 44.5°, 51.8° and 76.4° are assigned to the (111), (200) and (220) of face centered cubic (fcc) Ni.[20] Samples of Ni-NPs-1.4 and 1.8 also show the same XRD peaks (Fig. S5, ESI†). For the Ni 2p spectrum obtained by X-ray photoelectron spectroscopy (XPS, Fig. 2e and Fig. S6, ESI†), the main peaks at 855 and 873 eV are assigned to Ni $2p_{3/2}$ and $2p_{1/2}$, respectively. The Ni $2p_{3/2}$ peak can be fitted with Ni^0 at 851.8 eV and Ni^{2+} at 855.6 eV.[32] All the above results confirm that the main composition of Ni-NPs-1.6 is simply metallic Ni. The trace oxygen element in EDS mapping and the presence of oxidized Ni species in XPS spectrum is considered as the inevitable oxidation in the preparation for sample characterization.[36] In the high resolution transmission electron microscopy (HRTEM) images (Fig. S7, ESI†), the density of GB defects of the electrodeposited Ni NPs shows a peak for the sample obtained at −1.6 V, which is consistent with the nanograin size (Fig. S8b–d, ESI†) and suggests that the optimal electrodeposition potential for the formation of massive GB defects is −1.6 V (*vs.* SCE). The selected area electron diffraction (SAED) pattern in the inset of Fig. 2f and the HRTEM image (Fig. 2g and Fig. S9, ESI†) show a typical polycrystalline feature of fcc Ni. It is composed of numerous ordered nanograins with different orientations. Three fringes of different lattice planes of fcc Ni can be observed in the nanograins, namely the Ni(111), Ni(200) and Ni(220). On the edge of the nanograins, abundant GBs can be identified.[44,45] The STEM-HAADF image (Fig. 2h) shows one specific region of GB defects, in which the GB is seen to separate two nanograins (Ni(111) and Ni(111)). Fig. S10 (ESI†) also shows GB defects with triple junctions among Ni(111), Ni(200) and Ni(220). The strains induced by the GB defects were also characterized. The Williamson–Hall method was applied to calculate the average strains.[46–48] As shown in the fitted results (Fig. S8e–g, ESI†), the sample with a higher density of GBs displays a larger strain value. However, the strain calculated using the Williamson–Hall method contains no information about its location. Therefore, the geometric phase analysis (GPA) was further applied.[40] As can be observed from the figure of strain representation in the axial (ε_{xx}) and shear (ε_{xy}) directions (Fig. S8h, ESI†), the strain caused by the GB defects is mainly in the axial direction, which can be either in expansion or suppression. More importantly, the strain is mainly distributed along the GB region and on both sides of GB. Its value is as high as ~5%, much higher than that obtained from the XRD pattern. Compared to the GB area, the inside area of the grain represents a relatively lower strain value. Based on these results, we can conclude that the GB defects can indeed cause lattice strains. However, the strain is mainly at the GB region, *i.e.*, at the edge of each grain, whereas the inside area of the grain shows much lower strain values or even no strain.

2.3 Electrocatalysis performance and practical application demonstration

For these GB defect engineered Ni NPs, electrochemical nitrate reduction tests were conducted using a typical H-cell under ambient conditions to evaluate the contribution of the GB defects to the nitrate to ammonia conversion (Experiment details, ESI†). The main products of nitrate reduction including nitrite and ammonia were detected using colorimetric and/or ^{1}H nuclear magnetic resonance (^{1}H-NMR) (Fig. S11–S13, ESI†). LSV was conducted to measure the catalytic activities of different samples at a scan rate of 10 mV s^{-1} in an electrolyte of 1 M $NaNO_3$ + 1 M NaOH. Fig. 3a shows that the current density of carbon cloth deposited with GB defect engineered Ni NPs is significantly increased compared to that of bare carbon cloth. The highly positive onset potential of +0.3 V (*vs.* RHE) suggests a superior intrinsic activity for the nitrate to ammonia conversion using the GB engineered NPs. As the potential becomes more negative, massive bubbles were observed on the surfaces of Ni-NPs-1.8 at about −0.3 V. However, on the surfaces of Ni-NPs-1.4 and 1.6, almost no bubbles were observed even when the potential was increased to near −1 V and the current density was increased to larger than 2 A cm^{-2}. The results of LSV curves are consistent with the densities of the GB defects of different samples, indicating that such a nanostructure can effectively inhibit the HER and simultaneously promote the NitRR process. The Ni NPs with more GB defects also show a higher turnover frequency (TOF) (Fig. S14 and Tables S1, S2, ESI†).[49,50] The LSV curves normalized by the electrochemical surface area (ECSA) show similar trends, which confirms the superior intrinsic activity of the material (Fig. S15 and Table S3, ESI†). The LSV curves of Ni-NPs-1.6 at different electrodeposition durations suggest that 1400 s is the optimal time for the electrochemical reactions (Fig. S16, ESI†). The catalytic activities of Ni-NPs-1.6 at different nitrate concentrations were also investigated, and the results (Fig. S17, ESI†) show a gradual increase in the current density from 0.01 to 0.8 M, but nearly no changes with further increase in the concentration. Considering the consumption of reactants during electrocatalysis, a series of chronoamperometric measurements were carried out in an electrolyte of 1 M $NaNO_3$ + 1 M NaOH (Fig. S18–S20, ESI†). As can be observed from the results shown in Fig. 3b, the NH_3 rate of GB engineered Ni NPs is increased as the potential becomes more negative, and the value is significantly higher than that of the bare carbon cloth (Fig. S21 and S22, ESI†). Remarkably, the NH_3 rate of Ni-NPs-1.6 is as high as 15.49 mmol h^{-1} cm^{-2} at −0.93 V, which is mainly attributed to the abundant GB defects and large surface areas. The morphology and composition of this material are also maintained well after the experiments (Fig. S23–S26, ESI†). Moreover, the FE of Ni-NPs-1.6 is also excellent. From Fig. 3c, with the potential varied from −0.13 to −0.73 V, the reduction products are mainly NO_2^- and NH_3. At

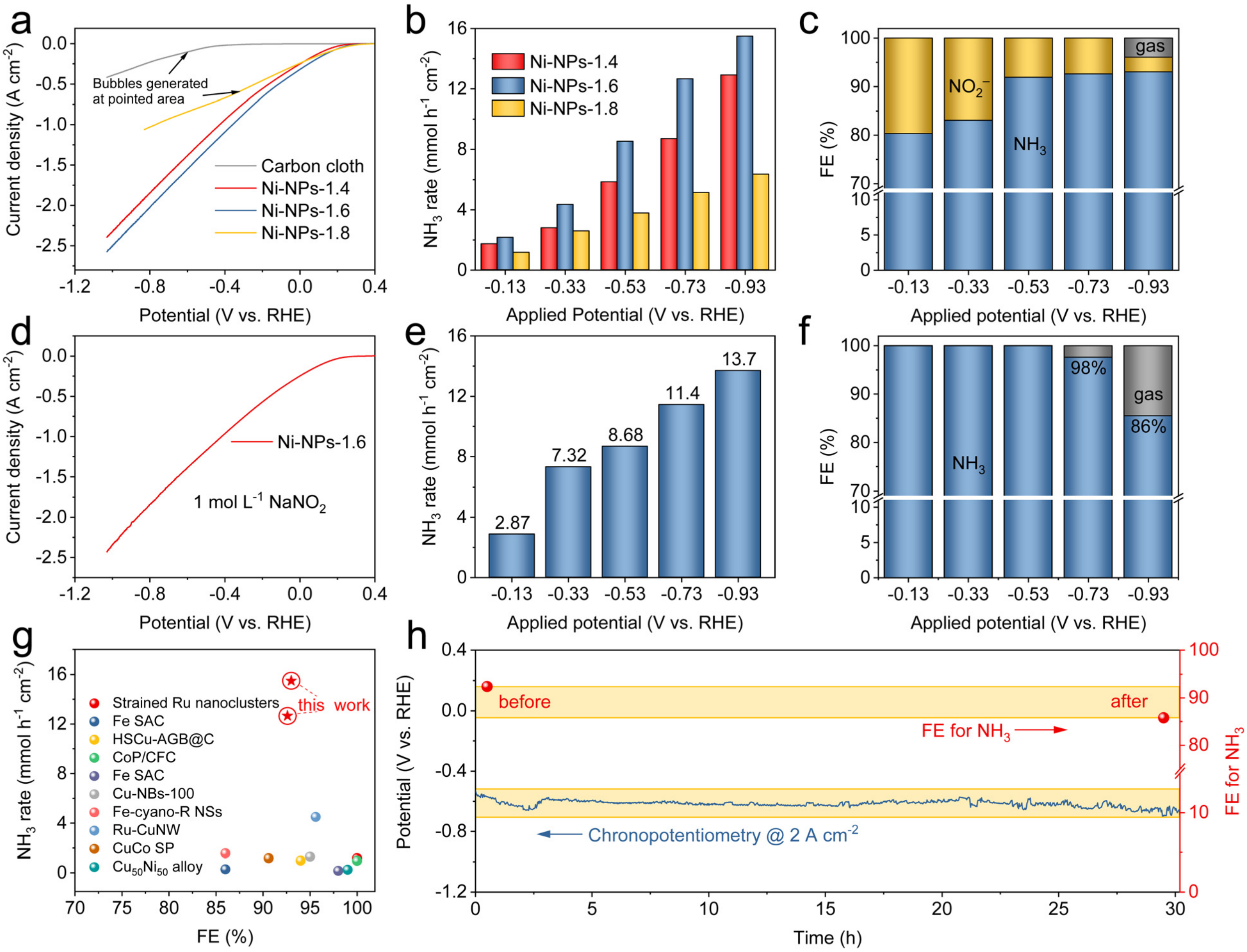

Fig. 3 (a) LSV curves of Ni-NPs-1.4, 1.6, and 1.8 and carbon cloth for nitrate reduction (1 M NaOH + 1 M $NaNO_3$). (b) NH_3 rate of Ni-NPs-1.4, 1.6 and 1.8 at different applied potentials. (c) Product distribution of Ni-NPs-1.6 under different applied potentials. (d) LSV curve of Ni-NPs-1.6 for nitrite reduction (1 M NaOH + 1 M $NaNO_2$). (e) NH_3 rate and (f) FE for ammonia of nitrite reduction at different applied potentials of Ni-NPs-1.6. (g) NH_3 rate and FE comparison of the as-synthesized Ni-NPs-1.6 with some reported electrocatalysts. (h) Stability experiment of Ni-NPs-1.6 *via* chronopotentiometry at 2 A cm^{-2} (blue line) and the FE for ammonia (red dot).

−0.93 V, about 4% gaseous products are produced, which are mainly H_2 or N_2,[51–53] while the FE for ammonia is still maintained larger than 90%. The small amount of gas product confirms that the GB defect engineered Ni NPs have an enhanced property on HER inhibition in a wide potential range, which is a guarantee for the high NH_3 rate and superior FE. The product compositions of Ni-NPs-1.4 and 1.8 at different applied potentials are illustrated in Fig. S27 and S28 (ESI†). The products of nitrate reduction of Ni-NPs-1.8 which has much less GB defects contain massive gas in a higher applied potential, which leads to a lower FE for ammonia. Moreover, the electrodeposited Ni NPs with abundant GB defects represent an enhanced NH_3 rate and superior HER inhibition compared to bulk Ni materials and chemically synthesized Ni materials (Fig. S29, ESI†). Such results confirm that the GB defects play a significant role in the suppression of the HER and the promotion of the NitRR.

The catalytic performance for nitrite reduction to ammonia was also investigated (Fig. 3d–f and Fig. S30, ESI†). As expected, the Ni-NPs-1.6 shows excellent performance. When the applied potential is changed from −0.13 to −0.53 V, the FE for ammonia is nearly 100%. If the potential is further increased to −0.93 V, the NH_3 rate can be increased to 13.7 mmol h^{-1} cm^{-2} with an FE value of 85.5%. The performance for both nitrate and nitrite reduction to ammonia in this study is much better than those of many reported catalysts (Fig. 3g and Tables S6 and S7, ESI†). A prolonged experiment was further performed to evaluate the catalytic stability of the Ni-NPs-1.6 under a high current density of 2 A cm^{-2}. The used testing system is illustrated in Fig. S31 (ESI†). As revealed from Fig. 3h, the Ni-NPs-1.6 shows outstanding stability over a period of 30 h, and the potential for ensuring the high current density of 2 A cm^{-2} shifts only slightly to a negative value. Surprisingly, throughout the 30 h experiment, very few bubbles were observed at the cathode. The FE for NH_3 production was slightly decreased from 92.4 to 85.8%, which confirms the excellent stability for HER inhibition and NitRR improvement if compared with those reported values in the literature (Fig. S32 and Table S4, ESI†). Such a high NH_3 rate and outstanding stability are promising for potential industrial applications.

To have an insight into the underlying mechanisms of nitrate reduction into ammonia, we also deposited the GB defect-rich Ni on a rotating disk electrode (RDE) to calculate the electron transfer number according to the Koutecky–Levich equation.[54]

$$\frac{1}{i}=\frac{1}{i_{\mathrm{k}}}+\frac{1}{0.62nFAD_0^{2/3}\omega^{1/2}\nu^{-1/6}C_0} \tag{1}$$

According to eqn (1), where i_{k} is the limiting current density (A cm^{-2}), n is the electron transfer number, F is the Faraday constant (96 485 C mol^{-1}), A is the specific area of the RDE (0.19625 cm^2), D_0 is the diffusion coefficient of the nitrate (1.80×10^{-5} $\mathrm{cm}^2\ \mathrm{s}^{-1}$),[55] ω is the rotation rate, ν is the kinematic viscosity (0.0118 $\mathrm{cm}^2\ \mathrm{s}^{-1}$),[20,56] and C_0 is the bulk concentration of nitrate (0.033×10^{-3} mol cm^{-3}). The inverse of current density i (A cm^{-2}) is proportional to the inverse of the square root of the rotation rate ($1/\omega^{1/2}$). The electron transfer number can be obtained through the slope of the fitted data. As shown in Fig. 4a and b, the platform of current density due to mass transfer limiting is increased with the rotation rate, since a higher rotation rate enhances the mass transfer progress. The electron transfer number of nitrate reduction increases from 2.6 to 5.3 as the potential shifts to a more negative value (Fig. S33 and Table S5, ESI†). Such results also correspond to the phenomena observed in experiments that the $\mathrm{NH_3}$ proportion in the reduction products of nitrate increases while the $\mathrm{NO_2^-}$ proportion decreases contrarily as the applied potential is increased to a more negative value.

The Tafel slope is an indicator of the rate determining step in the reduction of nitrate. We then further measured the Tafel slopes of different samples. All the obtained values are close to 120 mV dec^{-1} (Fig. 4c), confirming that the rate determining step is $\mathrm{NO_3^-}$ to $\mathrm{NO_2^-}$ conversion.[57] The order of one reaction can provide us with important information about its kinetic progress. The reaction rate order of $\mathrm{NO_3^-} + 8\mathrm{e^-} + 6\mathrm{H_2O} \rightarrow \mathrm{NH_3} + 9\mathrm{OH^-}$ can be calculated by fitting $\ln j$ (current density) with $\ln c$ (nitrate concentration) (Experiment details 1.3.3, ESI†).[31] The results in Fig. S34 (ESI†) show that the reaction rate order of Ni-NPs-1.6 is far away from 1 which has been widely reported in the literature.[16,58] Such results are due to the consequence of higher coverage of nitrate on the material,[11,31,32] suggesting that the $\mathrm{NO_3}$* can be strongly adsorbed on the surface of the catalyst. Favorable adsorption of nitrate is the precondition for efficient reduction.[11,31,32] The lower reaction order also suggests that the nitrate reduction on the surface of Ni-NPs-1.6 might be the radical participated reaction. To ensure that ammonia is the product of nitrate reduction rather than from the other sources, isotope tracing experiments were performed at −0.33 V (*vs.* RHE). ^{1}H-NMR spectroscopy shows two typical peaks of $^{15}\mathrm{NH_4^+}$ using $^{15}\mathrm{NO_3^-}$ instead of three peaks of $^{14}\mathrm{NH_4^+}$ when using $^{14}\mathrm{NO_3^-}$ as the N source,[59,60] which confirms that ammonia is the reduction product of $\mathrm{NO_3^-}$ (Fig. 4d).

Zn-nitrate battery is a recently proposed concept that combines energy output and ammonia synthesis in one system. Accordingly, the Zn-nitrate battery can not only be used as one battery system, but also treated as an electrocatalysis system to

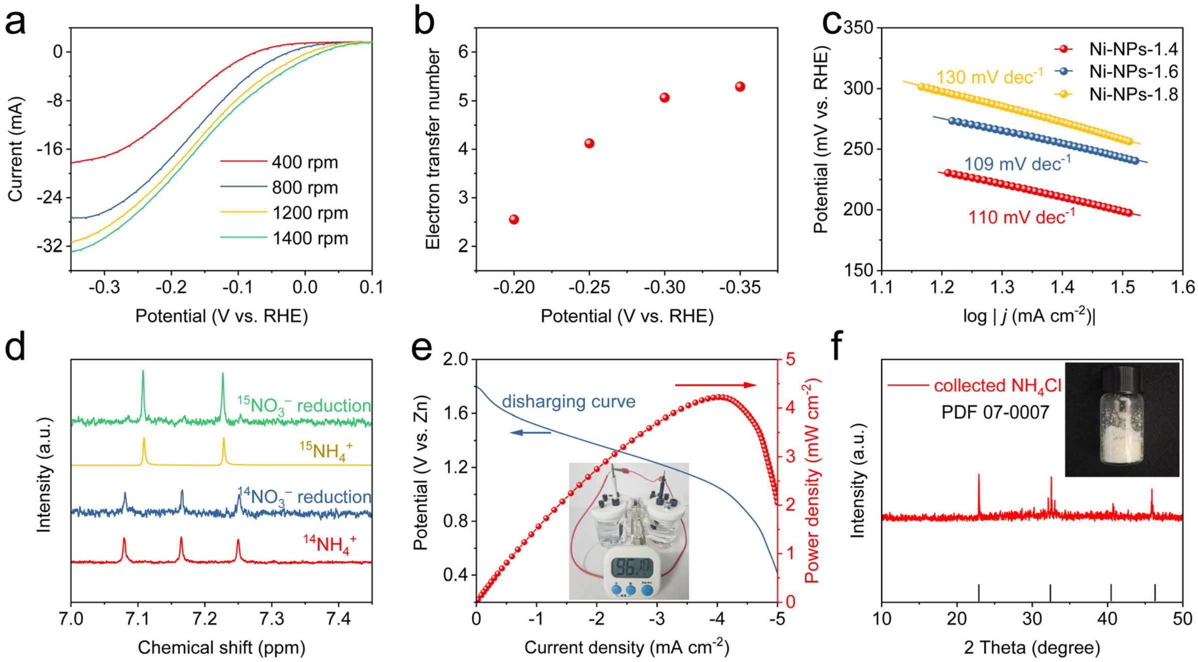

Fig. 4 (a) LSV curves under different rotation rates of Ni-NPs-1.6 deposited on a RDE and (b) the electron transfer number estimated using the Koutecky–Levich equation. (c) Tafel plots of the as-synthesized Ni-NPs-1.4, 1.6, and 1.8. (d) ^{1}H-NMR spectra of different electrolytes after catalysis when $^{15}\mathrm{NO_3^-}$ or $^{14}\mathrm{NO_3^-}$ is used as the N source and the spectra of $^{15}\mathrm{NH_4^+}$ and $^{14}\mathrm{NH_4^+}$ solution. (e) Discharging curve and power density of the two individual Zn-nitrate cells that are connected in series, and a photo of the electronic timer powered by this battery (the inset photo). (f) XRD pattern of the collected $\mathrm{NH_4Cl}$ and its photograph.

synthesize ammonia. Using the GB defect engineered Ni-NPs-1.6 as the anode and Zn foil as the cathode of one primary cell, we assembled a Zn-nitrate battery. Fig. 4e shows the discharge curve of the battery. It shows an increasing current density as the potential shifts negatively, and the power density has a peak of 4.2 mW cm^{-2}. The assembled battery can power an electronic timer (which is commonly used in daily life) for more than 2 days when two cells are connected in series. We also constructed a system (Fig. S31, ESI†) to simulate the industrial application of our material. The generated NH_3 was transferred into 0.3 M HCl to produce NH_4Cl, a commonly used fertilizer in agriculture. The collected NH_4Cl powder shows a typical white-pale yellow color, and its components could be confirmed by the XRD results (Fig. 4f). These results clearly demonstrate the capability for large-scale commercial applications of ammonia synthesis from nitrate reduction.

2.4 Proposed mechanism and DFT calculations

According to the literature, the dominant direct nitrate reduction mechanism can be generally divided into two specific pathways, *i.e.* adsorbed hydrogen-assisted and electron reduction pathways.[11,57] The migration of H* is much easier than that of N*, so the formation of the N–H bond is easier than that of N–N. As a result, the adsorbed hydrogen-assisted pathway is favorable for ammonia selectivity.[11] Nickel, one of the intensively investigated non-noble metals for the HER, has the potential to generate massive H* during water splitting, which can be considered a ''proton warehouse'' in nitrate reduction. Therefore, based on the results observed in the experiments, we propose a mechanism to explain the superiority of the as-synthesized material. Ni is an HER active metal, therefore, massive H* can be produced on its surface. However, as displayed in the LSV curves (Fig. 3a), very few bubbles were observed even though the overpotential for the HER was increased to near −1 V. Such an extraordinary phenomenon is attributed to that the produced H* is consumed by the intermediates in the NitRR process. To achieve this, the adsorption behavior of H* and nitrate (or the intermediates) should be appropriately regulated, so that H* can be easily transferred onto the NitRR pathway and simultaneously prevented from dissociation and formation of hydrogen. These synergistic effects are assumed to be the key factors for the superior performance of GB defect engineered Ni NPs.

To prove the above-proposed mechanism, we need to verify that the H* indeed exists and participates in the nitrate to ammonia conversion. We used D_2O to replace the H_2O as the solvent medium to evaluate the contribution of proton in the nitrate reduction. Fig. S35 (ESI†) shows that, as the proportion of deuterium increases the current density decreases, which clearly indicates that the proton can improve the catalytic activity of nitrate reduction into ammonia. The solvent kinetic isotope effect (SKIE) can be estimated using the ratio of current density in a pure protic medium ($NaOH + H_2O + NaNO_3$) and a pure deuterium medium ($NaOD + D_2O + NaNO_3$). As shown in Fig. 5a, the observed SKIE values are all larger than 1 and decreased as the applied potential shifts to a more negative value. Such a phenomenon is the consequence of more negative applied potential obscuring the reaction details. We also used a specific H* radical quenching reagent *tert*-butanol (TBA) to evaluate the role of active H*.[61] The current density became much lower when 200 or 600 μL of TBA was added (Fig. 5b), indicating that the H* radicals truly improved the reaction rate. We further used dimethyl-1-pyrroline-*N*-oxide (DMPO) as the radical trapping reagent to monitor the formation of H* radicals with and without using $NaNO_3$. As shown in Fig. 5c, the ESR spectra display typical 9 signals with intensity ratios of 1 : 1 : 2 : 1 : 2 : 1 : 2 : 1 : 1 without adding $NaNO_3$ in the catholyte, which confirms the formation of DMPO-H.[36] However, when $NaNO_3$ was added, the typical 9 signals disappeared, indicating that the produced H* is consumed by the intermediates in the NitRR process. These results strongly prove the key role of the H* radicals in nitrate reduction into ammonia.

In situ attenuated total reflectance Fourier transform infrared spectroscopy (ATR-FTIR) was also applied to distinguish the reaction pathway. As displayed in Fig. 5d, under the open circuit potential (OCP), no signals could be detected. When a more negative potential is applied, several peaks of the intermediates appear. The peak at 1240 cm^{-1} is assigned to the N–O antisymmetric stretching of NO_2^-,[62–65] which is one significant intermediate in the conversion of NO_3^- to NH_3 as it is related to the rate determining step. The peak at 1124 cm^{-1} is assigned to the N–O bond, the key intermediate in product selection.[64] The peaks located at ∼3350 cm^{-1} and ∼1630 cm^{-1} are attributed to the O–H stretching and the bending of H_2O,[64] which indicates that H_2O participated in the reaction because the proton in the H_2O molecule is needed in NH_3 production. The emergence of typical peaks of $-NH_2$ wagging mode at 1440 cm^{-1} and the N–H bending at 3682 cm^{-1} confirms the formation of NH_3.[64,66]

For further investigation of the mechanism, Density Functional Theory (DFT) calculations were performed. As displayed in the HRTEM image (Fig. 2g), the GB defect of Ni(111)–Ni(111) was the most observed one. Therefore, it was selected as the model for the DFT calculations (Fig. 5e and Fig. S36, ESI†).[67,68] The GB can be easily observed if the Ni atoms are displayed in smaller sizes. As a comparison, the structure of pristine Ni(111) was also built (Fig. 5e). We calculated the adsorption energy of the key species in the NitRR, *i.e.*, NO_3^-, NO_2^- and NH_3 on the pristine and GB Ni. As displayed in Fig. 5f, the adsorption of NO_3^- and NO_2^- on GB Ni is more favorable than that of pristine Ni, which contributes to a higher coverage of nitrate on the catalyst surface and leads to a lower reaction order, which is consistent with the results shown in Fig. S34 (ESI†). In contrast, the adsorption energy of NH_3 is relatively lower, and the produced NH_3 can be effectively dissociated from the catalyst surface, so that the active sites can be available for the next catalytic cycle. This contributes to a higher value of TOF, which is consistent with the results shown in Fig. S14 (ESI†). According to the detected intermediates using *in situ* ATR-FTIR and the previous reports,[69,70] the reaction pathway of $NO_3^- + 6H_2O + 8e^- \rightarrow NH_3 + 9OH^-$ was subdivided into two sequences, *i.e.*, (1) a continuous deoxidation process, $NO_3^* \rightarrow NO_2^* \rightarrow NO^* \rightarrow N^*$,

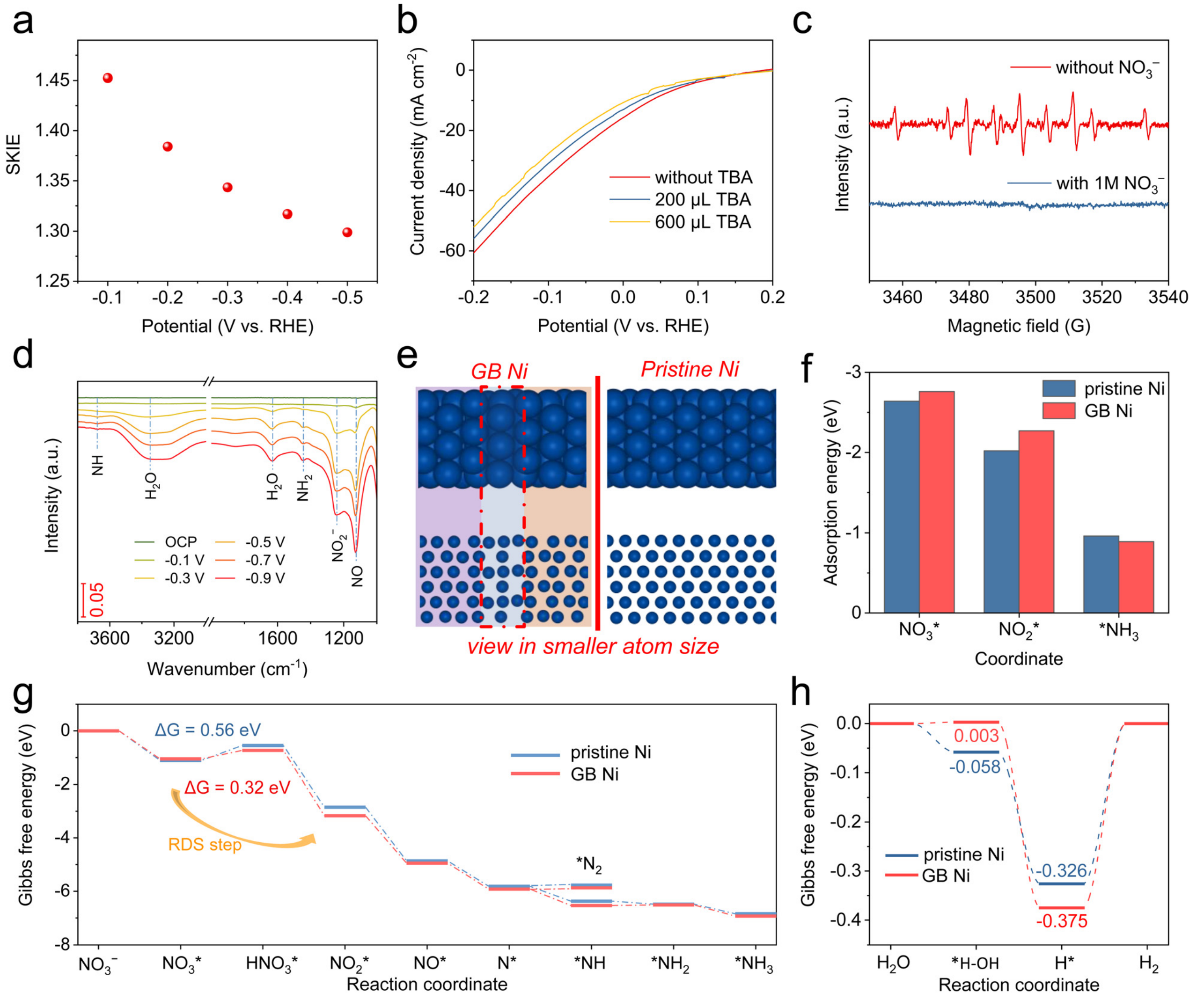

Fig. 5 (a) SKIE values under different applied potentials. (b) Different LSV curves of Ni-NPs-1.6 with or without TBA. (c) ESR spectra of the solution (with or without nitrate) obtained after 10 min electrocatalysis of Ni-NPs-1.6. (d) *In situ* ATR FTIR spectra of different intermediates in the NitRR pathway. (e) The built structure model of GB Ni and pristine Ni for DFT calculations. (f) Adsorption energy of three key species on GB Ni and pristine Ni. (g) Gibbs free energy diagrams of the full pathways for the conversion of nitrate to ammonia on pristine Ni and GB Ni. (h) Gibbs free energy diagrams of the full pathways for the HER on pristine Ni and GB Ni.

and (2) a continuous hydrogenation process, *N → *NH → *NH_2 → *NH_3. All the adsorption configurations of the intermediates on the GB Ni and pristine Ni are illustrated in Fig. S37 (ESI†). Based on all these results, we illustrate the nitrate reduction process on GB defect engineered nano-nickel (Fig. 5g) and show a complete electrocatalytic cycle in Fig. S38 (ESI†). During the nitrate reduction, NO_3^- is first adsorbed on the Ni atoms to form NO_3* *via* two-fold coordination,[71] which is then followed by the deoxidation process of NO_3* → NO_2*. This step is considered the rate determining step of nitrate reduction to ammonia, which can be confirmed by its Tafel slope of ~120 mV dec^{-1} (Fig. 4c).[20] On the GB Ni, H* is easier to combine with NO_3* and form HNO_3* with an energy barrier of 0.32 eV, which is beneficial for the conversion of NO_3* to NO_2*. After this RDS, the free energy shows a continuous downstep. The formation energy of N_2 is higher than that of N–H, which confirms a good selectivity of NH_3 on GB Ni. The free energy diagrams for the HER of GB Ni and pristine Ni were also calculated and are shown in Fig. 5h. The adsorption configurations are shown in Fig. S39 (ESI†). The higher energy barrier of H* → H_2 on GB Ni confirms a higher H* retention capacity. The produced H* cannot be easily released to form H_2, but be stored as a "proton warehouse" in the GB regions. Notably, the GB regions are also the adsorption sites for NO_3* and NO_2*. The energy barrier of NO_3* → HNO_3* → NO_2*, *i.e.*, the RDS in the NitRR, is lower than the energy barrier of H* → H_2. Therefore, the H* is easier to combine with NO_3* and accelerate the RDS rather than forming H_2, which confirms the good inhibition on the HER and the improvement of the NitRR for the as-synthesized material. The computational simulation results above can also strongly support the hypothesis.

3 Conclusions

In conclusion, we have presented a simple method to synthesize GB defect engineered Ni NPs, which can be applied as an efficient and selective catalyst for nitrate reduction to ammonia. Benefiting from the regulation of H* adsorption and the favorable adsorption for the intermediates in the NitRR pathway, the NH_3 production rate can be significantly accelerated, and the HER can be suppressed simultaneously. Owing to these synergistic effects, the as-synthesized catalyst exhibits a superior NH_3 rate of 15.49 mmol h^{-1} cm^{-2} with an outstanding FE value of 93.0%, which is much higher compared with those of many reported catalysts. This study offers a new methodology that the HER active material should not be overlooked in the catalyst design for the NitRR. The high NH_3 rate also makes a big step toward the practical applications of ammonia electrosynthesis and nitrate removal in the hydrosphere.

Author contributions

J. Zhou conceived this idea, conceptualized the work, designed and conducted the experiments, analysed and processed the data, wrote the original draft, and wrote the original response letter. Prof. M. Wen, Q.-S. Wu and Y.-Q. Fu supervised the research and made comments on the manuscript. Prof. G.-F. Wei conducted the DFT calculations. Prof. R. Huang conducted TEM characterization in revising the manuscript. Y.-K. Tian carried out part of the electrochemical test and the analysis of DFT simulation results. Y.-X. Luo conducted part of the sample characterization. Prof. Y.-Q. Fu modified the grammar.

Conflicts of interest

There are no conflicts to declare.

Acknowledgements

This work was financially supported by the National Natural Science Foundation (NSFC Nos: 22171212), the Science and Technology Committee of Shanghai Municipality (2116071 0300, 19DZ2271500, 2022-4-ZD-03, and 2022-4-YB-12) by China, and the International Exchange Grant (IEC/NSFC/201078) through Royal Society UK and NSFC. Thanks for the help in characterization and test from Ze-chen Wu, Zi-ning Wang, Jun Zhou, Chun-hui Wang and Prof. Wei-Ying Li of Tongji University.

Notes and references

1 R. Schlögl, *Angew. Chem., Int. Ed.*, 2003, **42**, 2004–2008.

2 T.-N. Ye, S.-W. Park, Y. Lu, J. Li, M. Sasase, M. Kitano, T. Tada and H. Hosono, *Nature*, 2020, **583**, 391–395.

3 P. H. van Langevelde, I. Katsounaros and M. T. Koper, *Joule*, 2021, **5**, 290–294.

4 Y. Wang, W. Zhou, R. Jia, Y. Yu and B. Zhang, *Angew. Chem., Int. Ed.*, 2020, **59**, 5350–5354.

5 J. W. Erisman, M. A. Sutton, J. Galloway, Z. Klimont and W. Winiwarter, *Nat. Geosci.*, 2008, **1**, 636–639.

6 Y. Zeng, C. Priest, G. Wang and G. Wu, *Small Methods*, 2020, **4**, 2000672.

7 J. Wang, T. Feng, J. Chen, V. Ramalingam, Z. Li, D. M. Kabtamu, J.-H. He and X. Fang, *Nano Energy*, 2021, **86**, 106088.

8 S. Garcia-Segura, M. Lanzarini-Lopes, K. Hristovski and P. Westerhoff, *Appl. Catal., B*, 2018, **236**, 546–568.

9 J. Martínez, A. Ortiz and I. Ortiz, *Appl. Catal., B*, 2017, **207**, 42–59.

10 M. Duca and M. T. M. Koper, *Energy Environ. Sci.*, 2012, **5**, 9726–9742.

11 Y. Wang, C. Wang, M. Li, Y. Yu and B. Zhang, *Chem. Soc. Rev.*, 2021, **50**, 6720–6733.

12 C. Milhano and D. Pletcher, *Modern Aspects of Electrochemistry, No. 45*, Springer New York, New York, NY, 2009, vol. 45, pp. 1–61.

13 P. Li, Z. Jin, Z. Fang and G. Yu, *Energy Environ. Sci.*, 2021, **14**, 3522–3531.

14 R. Daiyan, T. Tran-Phu, P. Kumar, K. Iputera, Z. Tong, J. Leverett, M. H. A. Khan, A. Asghar Esmailpour, A. Jalili, M. Lim, A. Tricoli, R.-S. Liu, X. Lu, E. Lovell and R. Amal, *Energy Environ. Sci.*, 2021, **14**, 3588–3598.

15 W.-J. Sun, H.-Q. Ji, L.-X. Li, H.-Y. Zhang, Z.-K. Wang, J.-H. He and J.-M. Lu, *Angew. Chem., Int. Ed.*, 2021, **60**, 22933–22939.

16 J. Wang, C. Cai, Y. Wang, X. Yang, D. Wu, Y. Zhu, M. Li, M. Gu and M. Shao, *ACS Catal.*, 2021, **11**, 15135–15140.

17 C. Wang, F. Ye, J. Shen, K.-H. Xue, Y. Zhu and C. Li, *ACS Appl. Mater. Interfaces*, 2022, **14**, 6680–6688.

18 X. Deng, Y. Yang, L. Wang, X.-Z. Fu and J.-L. Luo, *Adv. Sci.*, 2021, **8**, 2004523.

19 J. P. Troutman, H. Li, A. M. Haddix, B. A. Kienzle, G. Henkelman, S. M. Humphrey and C. J. Werth, *ACS Catal.*, 2020, **10**, 7979–7989.

20 Y. Wang, A. Xu, Z. Wang, L. Huang, J. Li, F. Li, J. Wicks, M. Luo, D.-H. Nam, C.-S. Tan, Y. Ding, J. Wu, Y. Lum, C.-T. Dinh, D. Sinton, G. Zheng and E. H. Sargent, *J. Am. Chem. Soc.*, 2020, **142**, 5702–5708.

21 C. Wang, Z. Liu, T. Hu, J. Li, L. Dong, F. Du, C. Li and C. Guo, *ChemSusChem*, 2021, **14**, 1825–1829.

22 Z.-X. Ge, T.-J. Wang, Y. Ding, S.-B. Yin, F.-M. Li, P. Chen and Y. Chen, *Adv. Energy Mater.*, 2022, **12**, 2103916.

23 H. Yin, Z. Chen, S. Xiong, J. Chen, C. Wang, R. Wang, Y. Kuwahara, J. Luo, H. Yamashita, Y. Peng and J. Li, *Chem Catal.*, 2021, **1**, 1088–1103.

24 L. Wei, D.-J. Liu, B. A. Rosales, J. W. Evans and J. Vela, *ACS Catal.*, 2020, **10**, 3618–3628.

25 Q. Yao, J. Chen, S. Xiao, Y. Zhang and X. Zhou, *ACS Appl. Mater. Interfaces*, 2021, **13**, 30458–30467.

26 S. Ye, Z. Chen, G. Zhang, W. Chen, C. Peng, X. Yang, L. Zheng, Y. Li, X. Ren, H. Cao, D. Xue, J. Qiu, Q. Zhang and J. Liu, *Energy Environ. Sci.*, 2022, **15**, 760–770.

27 T. Zhu, Q. Chen, P. Liao, W. Duan, S. Liang, Z. Yan and C. Feng, *Small*, 2020, **16**, 2004526.

28 J. Li, Y. Zhang, C. Liu, L. Zheng, E. Petit, K. Qi, Y. Zhang, H. Wu, W. Wang, A. Tiberj, X. Wang, M. Chhowalla, L. Lajaunie, R. Yu and D. Voiry, *Adv. Funct. Mater.*, 2022, **32**, 2108316.

29 H. Niu, Z. Zhang, X. Wang, X. Wan, C. Shao and Y. Guo, *Adv. Funct. Mater.*, 2021, **31**, 2008533.

30 Z.-Y. Wu, M. Karamad, X. Yong, Q. Huang, D. A. Cullen, P. Zhu, C. Xia, Q. Xiao, M. Shakouri, F.-Y. Chen, J. Y. Kim, Y. Xia, K. Heck, Y. Hu, M. S. Wong, Q. Li, I. Gates, S. Siahrostami and H. Wang, *Nat. Commun.*, 2021, **12**, 2870.

31 O. Q. Carvalho, R. Marks, H. K. K. Nguyen, M. E. Vitale-Sullivan, S. C. Martinez, L. Árnadóttir and K. A. Stoerzinger, *J. Am. Chem. Soc.*, 2022, **144**, 14809–14818.

32 W. Zheng, L. Zhu, Z. Yan, Z. Lin, Z. Lei, Y. Zhang, H. Xu, Z. Dang, C. Wei and C. Feng, *Environ. Sci. Technol.*, 2021, **55**, 13231–13243.

33 J. Li, G. Zhan, J. Yang, F. Quan, C. Mao, Y. Liu, B. Wang, F. Lei, L. Li, A. W. M. Chan, L. Xu, Y. Shi, Y. Du, W. Hao, P. K. Wong, J. Wang, S.-X. Dou, L. Zhang and J. C. Yu, *J. Am. Chem. Soc.*, 2020, **142**, 7036–7046.

34 J. Yu, Y. Qin, X. Wang, H. Zheng, K. Gao, H. Yang, L. Xie, Q. Hu and C. He, *Nano Energy*, 2022, **103**, 107705.

35 Y. Zhang, X. Chen, W. Wang, L. Yin and J. C. Crittenden, *Appl. Catal., B*, 2022, **310**, 121346.

36 H. Liu, X. Lang, C. Zhu, J. Timoshenko, M. Rüscher, L. Bai, N. Guijarro, H. Yin, Y. Peng, J. Li, Z. Liu, W. Wang, B. R. Cuenya and J. Luo, *Angew. Chem., Int. Ed.*, 2022, **61**, e202202556.

37 T. Zhu, S. Liu, B. Huang, Q. Shao, M. Wang, F. Li, X. Tan, Y. Pi, S.-C. Weng, B. Huang, Z. Hu, J. Wu, Y. Qian and X. Huang, *Energy Environ. Sci.*, 2021, **14**, 3194–3202.

38 Y. Tian, A. Huang, Z. Wang, M. Wang, Q. Wu, Y. Shen, Q. Zhu, Y. Fu and M. Wen, *Chem. Eng. J.*, 2021, **426**, 131827.

39 H. Fang, J. Yang, M. Wen and Q. Wu, *Adv. Mater.*, 2018, **30**, 1705698.

40 S. Hao, H. Sheng, M. Liu, J. Huang, G. Zheng, F. Zhang, X. Liu, Z. Su, J. Hu, Y. Qian, L. Zhou, Y. He, B. Song, L. Lei, X. Zhang and S. Jin, *Nat. Nanotechnol.*, 2021, **16**, 1371–1377.

41 L. Godeffroy, P. Ciocci, A. Nsabimana, M. Miranda Vieira, J.-M. Noël, C. Combellas, J.-F. Lemineur and F. Kanoufi, *Angew. Chem., Int. Ed.*, 2021, **60**, 16980–16983.

42 J. Ustarroz, J. A. Hammons, T. Altantzis, A. Hubin, S. Bals and H. Terryn, *J. Am. Chem. Soc.*, 2013, **135**, 11550–11561.

43 Z. Chen, T. Wang, B. Liu, D. Cheng, C. Hu, G. Zhang, W. Zhu, H. Wang, Z.-J. Zhao and J. Gong, *J. Am. Chem. Soc.*, 2020, **142**, 6878–6883.

44 S. Ye, J. Wang, J. Hu, Z. Chen, L. Zheng, Y. Fu, Y. Lei, X. Ren, C. He, Q. Zhang and J. Liu, *ACS Catal.*, 2021, **11**, 6104–6112.

45 C. Zhao, G. Luo, X. Liu, W. Zhang, Z. Li, Q. Xu, Q. Zhang, H. Wang, D. Li, F. Zhou, Y. Qu, X. Han, Z. Zhu, G. Wu, J. Wang, J. Zhu, T. Yao, Y. Li, H. J. Bouwmeester and Y. Wu, *Adv. Mater.*, 2020, **32**, 2002382.

46 G. Kim, H. Min, K. S. Lee, D. Y. Lee, S. M. Yoon and S. I. Seok, *Science*, 2020, **370**, 108–112.

47 S. Sarkar, S. D. Ramarao, T. Das, R. Das, C. P. Vinod, S. Chakraborty and S. C. Peter, *ACS Catal.*, 2021, **11**, 800–808.

48 D. Nath, F. Singh and R. Das, *Mater. Chem. Phys.*, 2020, **239**, 122021.

49 S. Anantharaj, P. E. Karthik and S. Noda, *Angew. Chem., Int. Ed.*, 2021, **60**, 23051–23067.

50 S. Anantharaj and S. Kundu, *ACS Energy Lett.*, 2019, **4**, 1260–1264.

51 H. Xu, H. Xu, Z. Chen, X. Ran, J. Fan, W. Luo, Z. Bian, W.-X. Zhang and J. Yang, *ACS Appl. Mater. Interfaces*, 2019, **11**, 3861–3868.

52 W. Teng, J. Fan and W.-X. Zhang, *ACS Appl. Mater. Interfaces*, 2020, **12**, 28091–28099.

53 C. Chen, K. Li, C. Li, T. Sun and J. Jia, *Environ. Sci. Technol.*, 2019, **53**, 13868–13877.

54 S.-E. Bae, K. L. Stewart and A. A. Gewirth, *J. Am. Chem. Soc.*, 2007, **129**, 10171–10180.

55 D. Pletcher and Z. Poorabedi, *Electrochim. Acta*, 1979, **24**, 1253–1256.

56 M. Chatenet, M. Molina-Concha, N. El-Kissi, G. Parrour and J.-P. Diard, *Electrochim. Acta*, 2009, **54**, 4426–4435.

57 H. Xu, Y. Ma, J. Chen, W.-X. Zhang and J. Yang, *Chem. Soc. Rev.*, 2022, **51**, 2710–2758.

58 W. Fu, X. Du, P. Su, Q. Zhang and M. Zhou, *ACS Appl. Mater. Interfaces*, 2021, **13**, 28348–28358.

59 S. Zhang, M. Li, J. Li, Q. Song and X. Liu, *Proc. Natl. Acad. Sci. U. S. A.*, 2022, **119**, e2115504119.

60 Y. Yu, C. Wang, Y. Yu, Y. Wang and B. Zhang, *Sci. China: Chem.*, 2020, **63**, 1469–1476.

61 Y. Wang, H. Li, W. Zhou, X. Zhang, B. Zhang and Y. Yu, *Angew. Chem., Int. Ed.*, 2022, **61**, e202202604.

62 O. Peng, Q. Hu, X. Zhou, R. Zhang, Y. Du, M. Li, L. Ma, S. Xi, W. Fu, Z.-X. Xu, C. Cheng, Z. Chen and K. P. Loh, *ACS Catal.*, 2022, **12**, 15045–15055.

63 E. Pérez-Gallent, M. C. Figueiredo, I. Katsounaros and M. T. M. Koper, *Electrochim. Acta*, 2017, **227**, 77–84.

64 J.-Y. Fang, Q.-Z. Zheng, Y.-Y. Lou, K.-M. Zhao, S.-N. Hu, G. Li, O. Akdim, X.-Y. Huang and S.-G. Sun, *Nat. Commun.*, 2022, **13**, 7899.

65 R. Zhang, S. Zhang, Y. Guo, C. Li, J. Liu, Z. Huang, Y. Zhao, Y. Li and C. Zhi, *Energy Environ. Sci.*, 2022, **15**, 3024–3032.

66 J.-Y. Ye, J.-L. Lin, Z.-Y. Zhou, Y.-H. Hong, T. Sheng, M. Rauf and S.-G. Sun, *J. Electroanal. Chem.*, 2018, **819**, 495–501.

67 J.-Q. Wang, C. Xi, M. Wang, L. Shang, J. Mao, C.-K. Dong, H. Liu, S. A. Kulinich and X.-W. Du, *ACS Catal.*, 2020, **10**, 12575–12581.

68 Q. Hu, Y. Qin, X. Wang, H. Zheng, K. Gao, H. Yang, P. Zhang, M. Shao and C. He, *CCS Chem.*, 2022, **4**, 2053–2064.

69 N. Zhang, J. Shang, X. Deng, L. Cai, R. Long, Y. Xiong and Y. Chai, *ACS Nano*, 2022, **16**, 4795–4804.

70 J.-X. Liu, D. Richards, N. Singh and B. R. Goldsmith, *ACS Catal.*, 2019, **9**, 7052–7064.

71 Z. Wang, D. Richards and N. Singh, *Catal. Sci. Technol.*, 2021, **11**, 705–725.